Coherence brightened laser source for atmospheric remote sensing

Andrew J. Traverso[a], Rodrigo Sanchez-Gonzalez[a], Luqi Yuan[a], Kai Wang[a], Dmitri V. Voronine[a,b], Aleksei M. Zheltikov[a,c], Yuri Rostovtsev[d], Vladimir A. Sautenkov[a], Alexei V. Sokolov[a], Simon W. North[a], and Marlan O. Scully[a,b,e,1]

[a]Texas A&M University, College Station, TX 77843; [b]Baylor University, Waco, TX 76798; [c]Moscow State University, Moscow 119992 Russia; [d]University of North Texas, Denton, TX 76203; and [e]Princeton University, Princeton, NJ 08544

Contributed by Marlan O. Scully, July 30, 2012 (sent for review May 7, 2012)

We have studied coherent emission from ambient air and demonstrated efficient generation of laser-like beams directed both forward and backward with respect to a nanosecond ultraviolet pumping laser beam. The generated optical gain is a result of two-photon photolysis of atmospheric O_2, followed by two-photon excitation of atomic oxygen. We have analyzed the temporal shapes of the emitted pulses and have observed very short duration intensity spikes as well as a large Rabi frequency that corresponds to the emitted field. Our results suggest that the emission process exhibits nonadiabatic atomic coherence, which is similar in nature to Dicke superradiance where atomic coherence is large and can be contrasted with ordinary lasing where atomic coherence is negligible. This atomic coherence in oxygen adds insight to the optical emission physics and holds promise for remote sensing techniques employing nonlinear spectroscopy.

nonadiabatic coherence | oxygen laser | coherence brightening | stand-off detection | intensity spiking

The need for an improved approach and efficient tools for remote optical sensing is apparent as they would facilitate applications ranging from environmental diagnostics and probing to chemical surveillance and biohazard detection. Present-day techniques rely on collecting incoherently scattered laser light and are often hindered by small signal collection efficiency (1–4). New emerging coherent techniques such as Raman (5, 6) and Terahertz (7) spectroscopies are promising. Availability of a laser-like light source emitting radiation in a controlled directional fashion, from a point in the sky back toward a detector, should revolutionize remote sensing (8, 9). Dogariu et al. demonstrated the possibility of remote lasing of atmospheric oxygen by using sub-mJ picosecond UV laser pulses at 226 nm that produce a bright near-infrared (NIR) laser source at 845 nm wavelength using atomic oxygen as the gain medium (10).

It has been proposed that a mirrorless laser can be used as a superradiant source where coherence is large, such as a coherence brightened laser (11–14). This type of superradiance was first demonstrated in optically pumped HF gas (15). Sweeping the gain, where multiple gain regions are used to stimulate each other, can enhance the superradiant emission (9). Gain-swept superradiance in air may be used to realize various nonlinear optical remote sensing schemes such as coherent Raman Umklappscattering (6), two-photon absorption (16), stimulated Raman scattering (17, 18), polarization Kerr effect (RIKES) spectroscopy (19), and others. Nonadiabatic coherence is a fundamental characteristic in coherence brightened emission processes like superradiance and superfluorescence and occurs when the macroscopic polarization of the medium changes more quickly than the decoherence rates. In the present paper, we study the temporal features of this NIR laser source from atomic oxygen and analyze the role of atomic coherence.

Stimulated emission (SE) in atomic oxygen—the key physical effect behind laser-like beam generation from UV-pumped atmospheric air—was first observed by Aldén et al. (20). They used 3 mJ, 5 ns, 226 nm laser pulses to simultaneously photodissociate molecular oxygen and excite the atomic oxygen product along the $2p^3P \rightarrow 3p^3P$ transition causing a population inversion and allowing for stimulated emission via the $3p^3P \rightarrow 3s^3S$ transition at 845 nm (20). This discovery initiated an in-depth examination of SE as a tool for flame and flow diagnostics in the early 1990s, including the analysis of laser-power and gas-pressure dependence of the SE signal (21) as well as the kinetics of the relevant populations (22).

Nearly two decades after the work on SE performed in the context of flame and flow diagnostics, a renewed interest in laser-like emission from open air is motivated by the need for chemically selective stand-off detection of trace gases in the atmosphere (8). Laser-like emission provides a promising tool for a broad class of all-optical stand-off detection methods, because it suggests a physical mechanism whereby a high-brightness, highly directional back-propagating light beam can be generated directly in ambient air. As proposed by earlier work on SE via femtosecond filamentation (23), the generation of backward-directed lasing in air, using the most dominant constituents such as nitrogen or oxygen, is very promising for remote atmospheric spectroscopy.

Time-resolved studies of SE pulse shapes on a picosecond time scale revealed an exponential decay of the SE signal in the wake of a picosecond UV pump pulse (24). In experiments with nanosecond pump pulses, the SE waveform was found to exhibit a spiky structure, which was attributed to a similar structure of the pump (24). Our own investigations also show a SE waveform with a spiky structure, but these spikes cannot be explained by the mechanisms previously proposed and may have a more profound physical significance. We demonstrate below that the spiky structure of SE pulses in our experiment may point toward nonadiabatic atomic coherence within the light emission process due to a large Rabi frequency and the very short time duration of the individual intensity spikes.

Experimental Procedure

General Emission Characteristics. In this work, we investigate the forward and backward directed emission of oxygen when pumped by nanosecond UV laser pulses. The experimental scheme is sketched in Fig. 1. The laser system consists of 532 nm output from an injection-seeded Spectra Physics PRO-290-10 Nd:YAG laser, which pumps a Sirah Cobra Stretch pulsed dye laser producing 622 nm output when a mixture of Rhodamine 610 and Rhodamine 640 in methanol is used. This 622 nm output is mixed with the residual 355 nm from the Nd:YAG laser in a Sirah SFM-355 frequency mixing unit to produce approximately 10 ns pulses of 226 nm light with approximately 10 mJ/pulse at 10 Hz (25).

Author contributions: A.V.S., S.W.N., and M.O.S. designed research; A.J.T., R.S.-G., L.Y., K.W., D.V.V., A.M.Z., Y.R., V.A.S., A.V.S., S.W.N., and M.O.S. performed research; A.J.T., L.Y., K.W., D.V.V., A.M.Z., Y.R., V.A.S., A.V.S., S.W.N., and M.O.S. analyzed data; and A.J.T., L.Y., D.V.V., A.V.S., and M.O.S. wrote the paper.

The authors declare no conflict of interest.

[1]To whom correspondence should be addressed. E-mail: scully@tamu.edu.

This article contains supporting information online at www.pnas.org/lookup/suppl/doi:10.1073/pnas.1211481109/-/DCSupplemental.

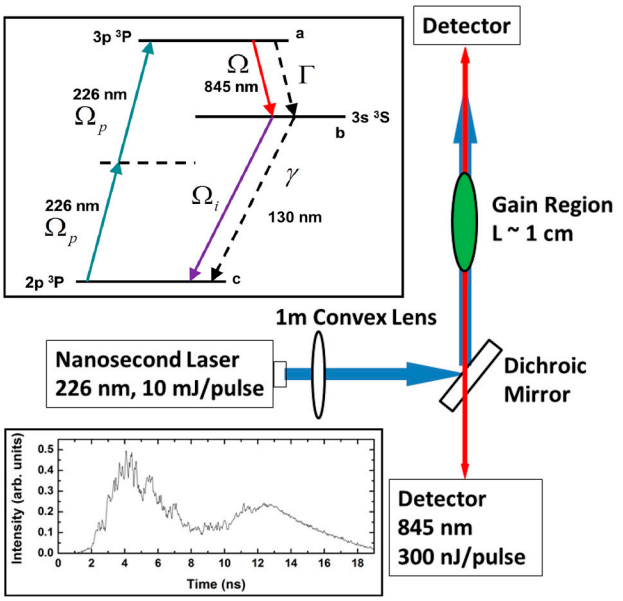

Fig. 1. Simplified experimental scheme. Nanosecond 226 nm laser pulses were focused with a 1 m lens dissociating the oxygen molecules at the focal point in ambient air. The 226 nm pulse further excited the newly dissociated oxygen atoms via two-photon absorption causing a population inversion. The backward detection was performed through a dichroic mirror. (*Bottom Inset*) An example of the pump pulse's intensity profile. (*Top Inset*) The energy level scheme is depicted for oxygen atoms undergoing two-photon excitation and stimulated emission at 845 nm. $\Gamma = 9.3 \times 10^6$ s^{-1} and $\gamma = 0.197 \times 10^9$ s^{-1} are the decay rates from $3p\ ^3P$ to $3s\ ^3S$ and from $3s\ ^3S$ to $2p\ ^3P$ states, respectively.

The resulting beam is focused using a convex lens (1-m focal length). The gain region, consisting of oxygen atoms produced by the focused pump, is approximately 1 cm long and has a waist of approximately 17 μm (see *SI Text* for more details). Emission in both the forward and backward direction is then detected and characterized. Particularly, a 300 nJ signal is detected in the backward direction.

The power of both signals was measured versus the pump power using a pyroelectric power meter from Ophir (Fig. 2*B*). A characteristic threshold behavior is observed for both forward and backward 845 nm beams indicating a laser-like process instead of simple fluorescence. Also, there was a distinct energy difference between the forward and backward emission, which is discussed below.

Furthermore, using the measured pulse energy, the average Rabi frequency can be experimentally estimated via $\Omega = \frac{\wp E}{\hbar}$, where E is the electric field amplitude and $\wp$ is the electric dipole moment, which depends on the spontaneous decay rate, Γ, according to $\wp = \sqrt{3\pi\varepsilon_0\hbar c^3\Gamma/\omega^3}$, where ω is the transition frequency (26). Given that $\Gamma = 9.3 \times 10^6$ s^{-1} for the $3p\ ^3P$ to $3s\ ^3S$ transition, $\wp = 1.41 \times 10^{-29}$ C·m. Similarly, the measured pulse energy (Fig. 2*B*) along with the diameter of the gain region and the pulse duration ($t \sim 10$ ns, discussed in next section), provide the average intensity $I = 6.11 \times 10^{10}$ W/m^2, which is then used to calculate the electric field amplitude via $I = n\varepsilon_0 c|E|^2/2$, where n is the index of refraction. This finally leads to an experimental estimate of the average Rabi frequency for the 845-nm transition $\Omega = 1.3 \times 10^{12}$ rad/s, whose high value provides further evidence of nonadiabatic atomic coherence when compared with the collisional dephasing rate ($\gamma_{col} \sim 1 \times 10^{10}$ s^{-1}) (27). In this case the average Rabi frequency is much higher than the dephasing rate, and when a system is in this regime, then atomic coherence effects will occur (28).

Further evidence of a laser-like process was discovered by analyzing the spatial beam profiles of the backward pulse when the pump power was varied from approximately 6 to 10 mJ. These measurements were made using a Spiricon beam profiler (SP620U). A distinct threshold was observed at approximately 8 mJ with a Gaussian profile. The width of the beam profile right at the threshold (8 mJ) was significantly wider than the profiles for any of the pump powers above threshold. Fig. 2*A* depicts this. Furthermore, from 6 to 8 mJ, emission was observed by eye, but the profile was too broad and weak for detection. Also, above threshold, all of the beam profiles had approximately the same width. Both of these features are indicative of a laser-like source.

Temporal Pulse Analysis. The temporal pulses shapes were measured using a Tektronix MSO72004C fast oscilloscope (20 GHz bandwidth, 50 GigaSamples/s, and approximately 20 ps resolution) and a New Focus high speed photodiode (model: 1,437; 25 GHz bandwidth and 14 ps rise time). As can be seen in Fig. 3, the temporal profiles varied from shot to shot mainly due to the rapid intensity fluctuations in the individual 226 nm pump pulses (an example is shown in the bottom inset of Fig. 1). Due to instrumental artifacts centered around 20 GHz, near the oscilloscope's bandwidth limit, all frequency components above 15 GHz were removed. Single-shot temporal profiles of forward and backward pulses were measured simultaneously using the same photodiode (New Focus, described above) and are presented in Fig. 3 *A* and *B*, respectively. The main feature of the temporal profiles is the high frequency oscillation, which is similar to spik-

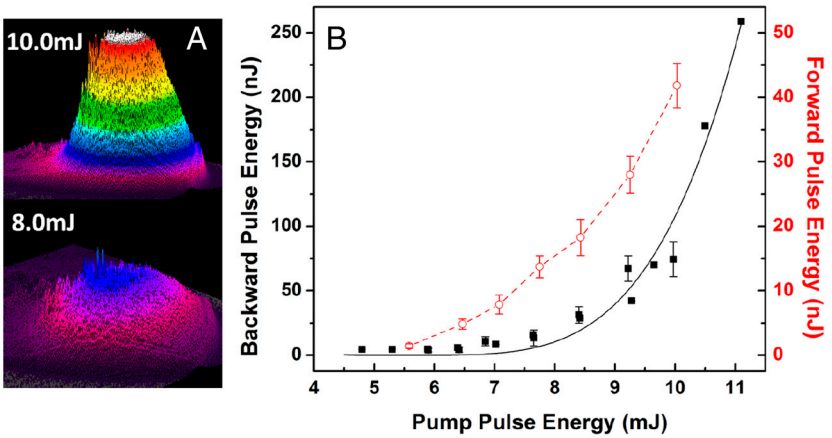

Fig. 2. (*A*) Spatial beam profiles of the 845 nm emitted backward pulse at pump energies above (10.0 mJ) and at (8.0 mJ) threshold. (*B*) The energy per pulse of both the forward (red circles) and backward (black squares) signals versus the pump power.

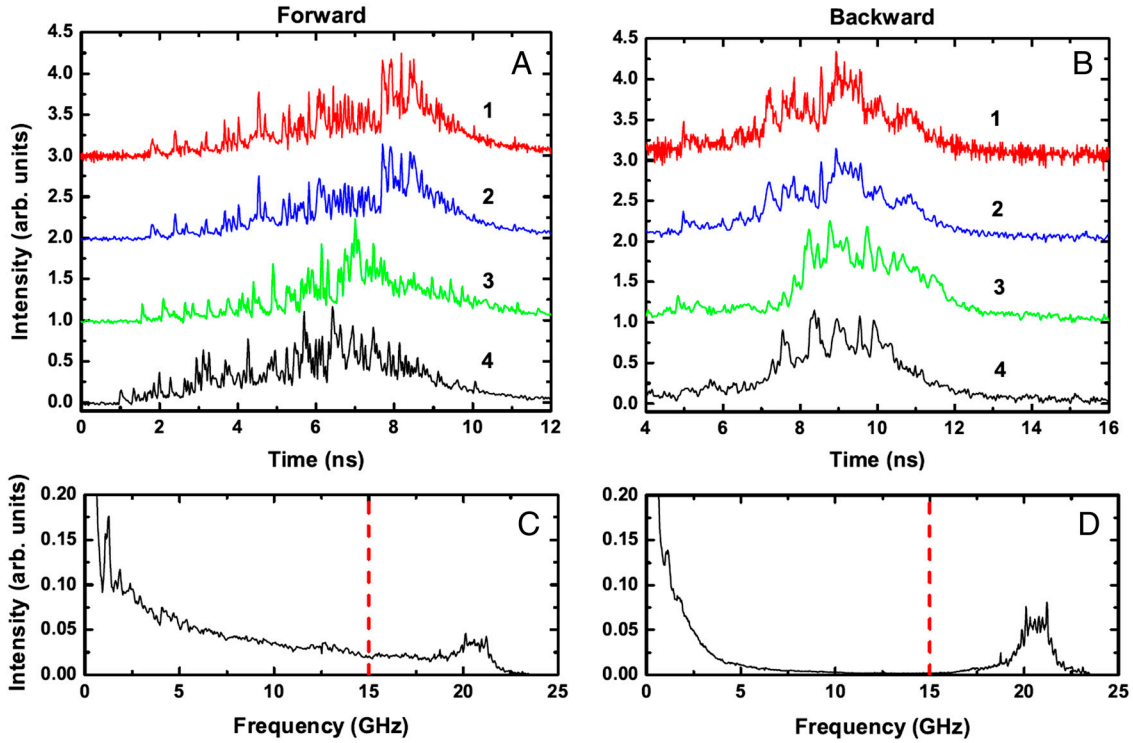

Fig. 3. Single shot temporal profiles of both forward (*A*) and backward (*B*) pulses at full pump energy (10 mJ). The top pulses, **1**, in both are shown without any frequency filtering while the pulses immediately below, **2**, are the same pulses after Fourier filtering. Pulses **3** and **4** are other examples of filtered pulses, vertically shifted for convenience. Averaged Fourier transforms of the forward (*C*) and backward (*D*) pulses. The Fourier transforms depict and help quantify spectral intensity modulations for both pulses. Filtering was applied by subtracting the Fourier spectrum of the background as well as removing all frequency components beyond the red dashed line as they were artifacts of the electronics.

ing that was previously observed and believed to be caused by intensity fluctuations in the pump pulse (24). In contrast to this previous experiment, our observed spiky structure is higher in both frequency and amplitude. Besides the rapid oscillations, several other features can be discerned from the data. Namely, the forward signal exhibits a higher rate of oscillation with more high frequency components (broadband, 5–15 GHz), as can be seen in the Fourier transforms in Fig. 3 *C* and *D*. Furthermore, from shot to shot, there are significant variations in the amplitude and number of oscillations.

In Fig. 4, we compare the typical narrowest spikes in the emitted pulses with a measured response of a femtosecond test pulse (Ti:Sapphire, 35 fs, 800 nm), which is well below the resolution limit. As can be seen in Fig. 4*A*, the forward spiking is most likely narrower than can be resolved by our detection system. In contrast, the narrowest peaks observed in the backward direction are approximately 60 ps (FWHM) in duration (Fig. 4*B*). These measurements along with the Fourier transforms depicted in Fig. 3 *C* and *D*, emphasize the distinction between the forward and backward emission, as well as differentiate these results from previous experiments where no difference between forward and backward spike duration was observed (24). Also, given how narrow these spikes are, it is clear that the peak Rabi frequency is higher than the average measured Rabi frequency, which extends this experiment further into the regime of strong nonadiabatic atomic coherence (28).

Model

On average, the width of the short spiking/ringing is less than 0.1 ns and 0.3 ns for the forward and backward pulses, respectively. These values can be compared to the estimated decay time for the system, which suggests the approximate time scale of intensity oscillations if atomic coherence is present. The characteristic delay, T_D and radiation damping time, T_R, of the collective system are given by refs. (29) and (30)

$$T_R = T_{sp}(8\pi/N\lambda^2 L), \quad [1]$$

$$T_D = \frac{T_R}{4}\left[\ln(\sqrt{2\pi NAL})\right]^2, \quad [2]$$

where $T_{sp} \sim 100$ ns is the spontaneous emission decay time for the lasing transition, $N \sim 10^{15}$ cm^{-3} is the density of the excited oxygen atoms in the gain region, $\lambda = 845$ nm is the wavelength of

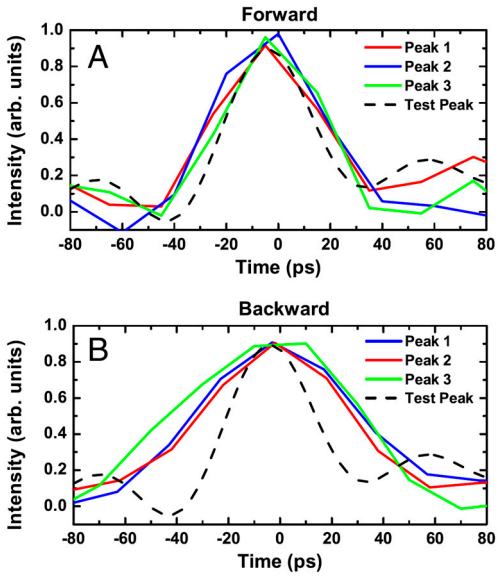

Fig. 4. Typical individual spikes for both the forward (*A*) and backward (*B*) pulses. In both figures, the dashed trace, Test Peak, is the response function of a 35 fs pulse at 800 nm used to test the resolution limit of the detection system. All traces are normalized for ease of comparison.

the emitted field, $A \sim 10^{-5}$ cm^2 is the cross-section of the gain region, and $L = 1$ cm is the gain length. Given these parameters, T_R is approximately 0.4 ps, which is much less than any other characteristic time scale that enters the problem (such as decoherence or dephasing time). $T_D \sim 15$ ps describes the amount of time needed to develop the initial atomic coherence but does not necessarily describe the time between the spikes. Furthermore, the single pass gain can be estimated using the above parameters as well as an experimentally estimated collisional dephasing rate, $\gamma_{col} \sim 10^{10}$ s^{-1} (27, 31). This gives a value of $\alpha L \sim 476$ where αL is the single pass gain, which places this experiment in the strong oscillatory superfluorescence regime (α is the gain coefficient, L is the length of the gain region) (31). While these values provide insight, a theoretical model is needed to provide a better understanding. This model and subsequent simulations are described below.

In order to model the problem, we write the semiclassical Hamiltonian of the atomic oxygen system in the interaction picture as

$$H = -\hbar\Omega_p e^{-i\Delta t}|a\rangle\langle b| - \hbar\Omega_p e^{i\Delta t}|b\rangle\langle c| - \hbar\Omega|a\rangle\langle b| - \hbar\Omega_i|b\rangle\langle c| + H.c., \quad [3]$$

where a, b, and c represent the levels $3p\ ^3P$, $3s\ ^3S$, and $2p\ ^3P$, respectively, in the oxygen atom in Fig. 1; whereas Ω_p, Ω, and Ω_i are the Rabi-frequencies of the 226 nm 2-photon pump pulse, the 845 nm signal, and the 130 nm field between the middle $3s\ ^3S$ state and the ground $2p\ ^3P$ state, respectively; Δ is the detuning from the $3s\ ^3S$ state for the two photon excitation from the $2p\ ^3P$ to the $3p\ ^3P$ state. With this Hamiltonian, we can derive the density matrix equations, which, in conjunction with the field propagation equations, are used to describe the evolution of the population, electric fields, and the atomic coherence. The density matrix approach is necessary because nonadiabatic coherence cannot be described by laser rate equations due to the macroscopic polarization evolving faster than all the decoherence rates in the system (28, 32). (The full set of equations is given in *SI Text*.)

The dephasing of the atomic dipoles plays an important role, because it depletes the coherence but not the state populations; we take $\gamma_{col} = 1 \times 10^{10}$ s^{-1} as above. It should be noted that the 130 nm UV field is coupled to the coherence between the excited state $3p\ ^3P$ and the intermediate state $3s\ ^3S$ for the forward 845 nm pulse but not for the backward pulse. This is due to the fact that the 130 nm spontaneous emission gets absorbed by the surrounding atmosphere too quickly to start any such amplification, but the forward 845 nm field, Ω_{ab}^{+}, has phase $ik_{ab}z$ and the coherence, ρ_{ac}, has phase $2ik_{pump}z$. With these fields, a phase-matching condition is satisfied for 130 nm emission in the forward direction, $2k_{pump} = k_{ab} + k_{bc}$. This is similar to yoked superfluorescence (33, 34). This coupling affects the coherence while the 130 nm field depletes the population in the intermediate state.

Using this theoretical framework, a one-dimensional simulation was performed assuming a fixed population of atoms that is uniformly distributed throughout the gain region. A smooth pump pulse resembling those found in the experiment (Fig. 1) was used as the initial input for the simulations; i.e. it was fit to the averaged pump pulse to mimic the overall pulse shape but lacked any rapid intensity oscillations. The results of the theoretical simulations are shown as curves **1** in Fig. 5 *A* and *B*. Despite the absence of rapid intensity oscillations in the pump, the simulations reveal rapid intensity oscillations with spike widths on the same order as those found experimentally. Essentially, the generated field becomes so strong that the corresponding time scale for the evolution of the atomic system becomes faster than dephasing.

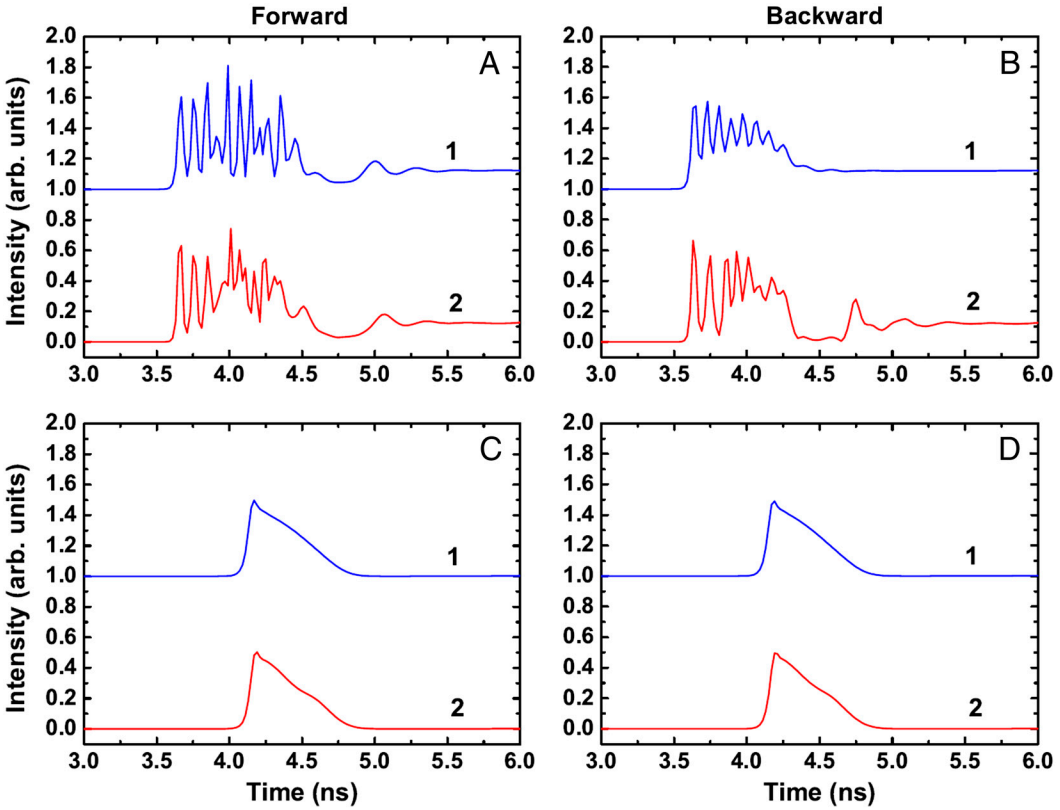

Fig. 5. Simulated forward (*A*) and backward (*B*) signals with a dephasing rate of $\gamma_{col} = 1 \times 10^{10}$ s^{-1}; forward (*C*) and backward (*D*) signals with artificially large collisional dephasing ($\gamma_{col} = 1 \times 10^{11}$ s^{-1}). Curves **1** (blue) are obtained using a smooth pump pulse as the initial input, while **2** (red) used a pump pulse with random intensity fluctuations to mimic the experiment. The curves are vertically shifted for convenience.

To substantiate that nonadiabatic atomic coherence phenomena are present, another simulation using the same theoretical model was constructed with an artificially large dephasing rate of $\gamma_{col} = 1 \times 10^{11}$ s^{-1} (curves **1** in Fig. 5 *C* and *D*). The large dephasing depletes the coherence in the 845 nm infrared transition but has no effect on the population. As such, the model predicts a simple pulse, akin to an ordinary laser pulse, with no high frequency modulations for both the forward and backward directions. Fig. 5 shows that the lack of coherence mitigates rapid oscillations which are characteristic of nonadiabatic coherence (11). The pulses seen in curves **1** of Fig. 5 *C* and *D* are due to laser spiking/relaxation oscillations (14). In fact, under the condition of large collisional dephasing, the density matrix equations reduce to the laser rate equations. Hence the observation of high frequency oscillations in both the theoretical results in curve **1** of Fig. 5 *A* and *B* and the experimental measurements in Fig. 3 *A* and *B* show the coherent dynamics associated with the reabsorption and reemission of the 845 nm light as the pulses propagate through the gain region. Experimentally, an order of magnitude increase in the collisional dephasing rate to $\gamma_{col} = 1 \times 10^{11}$ s^{-1} could be achieved by increasing the pressure of the gain medium. Further experiments with a gas cell under variable pressure could be used to explore this effect.

Further theoretical simulations were performed to verify the presence of nonadiabatic coherence. In particular, rapid intensity fluctuations were added to the pump pulse to resemble the experimental pump pulse shape. This was done to test whether pump fluctuations could cause the observed rapid spiking seen in our emitted pulses as had been seen previously (24). These simulations were again performed in both the small and artificially large collisional dephasing limits. For small collisional dephasing, rapid intensity spiking is still observed (curves **2** in Fig. 5 *A* and *B*), but it is quite apparent that the pump fluctuations do effect the rapid oscillations found in the emitted pulses. However it does not rule out atomic coherence. Rapid intensity oscillations must also appear in the emitted pulses at large dephasing for pump pulse fluctuations to be the main explanation of the phenomenon. In this regime (curve **2** of Fig. 5 *C* and *D*), all rapid oscillations disappear and the pulse shapes are similar to the large dephasing regime for the smooth pump pulse. This is consistent with attribution of the large amplitude rapid oscillations to a large atomic coherence.

Discussion

Again, the observed average Rabi frequency, $\Omega \sim 10^{12}$ rad/s, is more than an order of magnitude larger than the estimated dephasing rate $\gamma_{col} = 1 \times 10^{10}$ s^{-1}. Furthermore, the peak Rabi frequency is higher than the average as evidenced by the very short time scale of the intensity spiking (Fig. 4). These two results are strong evidence that places the emission process into the regime of nonadiabatic atomic coherence (28, 31).

The simulations performed above are intended to provide a qualitative insight into the physics of the emission process in ambient air. The model assumes the gain region to be one dimensional and populated uniformly by a fixed number of oxygen atoms and because of these assumptions does not reproduce the exact experimental findings (for example the pulse duration and the pulse energy difference). These discrepancies are likely caused by asymmetries in the gain region, which may occur in the experiment due to the molecular oxygen dissociation process and the non-Gaussian beam profile of the pump pulse. However, even with the above simplifications, the simulations do explain qualitatively the coherent nature of the observed intensity spikes on the temporal pulses. From the simulations, it is clear that the spiking only occurs when atomic coherence is present. In the case of small atomic coherence, i.e. when collisional dephasing is large, these rapid spikes are suppressed.

These results provide another step towards the implementation of stand-off spectroscopy of gases in the atmosphere. The high beam quality, stability, and power will allow detection of impurities in air with high sensitivity. In fact, this coherent emitted beam with a nanosecond pulse duration will be advantageous in nonlinear optical processes. It should provide higher peak intensity, which is crucial for techniques such as counter-propagating two-photon absorption, stimulated Raman scattering, or Raman-induced Kerr effect spectroscopies. The 845 nm wavelength is in a suitable range of most common realizations of these techniques for detecting vibrational fingerprints of relevant molecules.

ACKNOWLEDGMENTS. This work was supported by the Robert A. Welch Foundation (A-1261, A-1405, A-1547), the Office of Naval Research, National Science Foundation Grant EEC-0540832 (MIRTHE ERC), US Air Force Office of Scientific Research (Contract FA9550-04-1-0425; John Schmisseur, Program Manager), and the Army Research Office (Grant W911NF-07-1-0475). A.J.T., L.Y., and K.W. are supported by the Herman F. Heep and Minnie Belle Heep Texas A&M University Endowed Fund held/administered by the Texas A&M Foundation.

1. Steinbrecht V, Rothe KW, Walther H (1989) Lidar setup for daytime and nighttime probing of stratospheric ozone and measurements in polar and equatorial regions. *Appl Opt* 28:3616–3624.
2. Bisson SE, Goldsmith JEM, Mitchell MG (1999) Narrow-band, narrow-field-of-view Raman lidar with combined day and night capability for tropospheric water-vapor profile measurements. *Appl Opt* 38:1841–1849.
3. Rohwetter P, et al. (2004) Remote LIBS with ultrashort pulses: Characteristics in picosecond and femtosecond regimes. *J Anal At Spectrom* 19:437–444.
4. Plutov DV, Killinger DK (2010) Modeling of spectral emission-based lidar remote sensing. *Proc SPIE* 7665:76650D.
5. Li H, et al. (2009) Standoff and arms-length detection of chemicals with single-beam coherent anti-Stokes Raman scattering. *Appl Opt* 48:B17–B22.
6. Yuan L, et al. (2011) Coherent Raman Umklappscattering. *Laser Phys Lett* 8:736–741.
7. Liu J, Dai J, Chin SL, Zhang X-C (2010) Broadband terahertz wave remote sensing using coherent manipulation of fluorescence from asymmetrically ionized gases. *Nat Photon* 4:627–631.
8. Hemmer PR, et al. (2011) Standoff spectroscopy via remote generation of a backward-propagating laser beam. *Proc Natl Acad Sci USA* 108:3130–3134.
9. Kocharovsky V, et al. (2005) Gain-swept superradiance applied to the stand-off detection of trace impurities in the atmosphere. *Proc Natl Acad Sci USA* 102:7806–7811.
10. Dogariu A, Michael JB, Scully MO, Miles RB (2011) High-gain backward lasing in air. *Science* 331:442–445.
11. Dicke RH (1964) The coherence brightened laser. Quantum Electronics. *Proceedings of the third international congress*, eds P Grivet and N Bloembergen (Dunod Éditeur, Paris) p 35.
12. Dicke RH (1954) Coherence in spontaneous radiation processes. *Phys Rev* 93:99–110.
13. Lvovsky AI (1998) Omnidirectional superfluorescence transients. Ph.D. Thesis (Columbia University, New York).
14. Siegman AE (1986) *Lasers* (University Science Books, Sausalito, CA).
15. Skribanowitz N, Herman IP, MacGillivray JC, Feld MS (1973) Observation of Dicke superradiance in optically pumped HF gas. *Phys Rev Lett* 30:309–312.
16. Kaiser W, Garrett CGB (1961) Two-photon excitation in $CaF^2:Eu^{2+}$. *Phys Rev Lett* 7:229–231.
17. Shapiro SL, Giordmaine JA, Wecht KW (1967) Stimulated Raman and Brillouin scattering with picosecond light pulses. *Phys Rev Lett* 19:1093–1095.
18. Maier M, Kaiser W, Giordmaine JA (1969) Backward stimulated Raman scattering. *Phys Rev* 177:580–599.
19. Heiman D, Hellworth RW, Levenson MD, Martin G (1976) Raman-induced Kerr effect. *Phys Rev Lett* 36:189–192.
20. Aldén M, Westblom U, Goldsmith JEM (1989) Two-photon-excited stimulated emission from atomic oxygen in flames and cold gases. *Opt Lett* 14:305–307.
21. Westblom U, Agrup S, Aldén M, Hertz HM, Goldsmith JEM (1990) Properties of laser-induced stimulated emission for diagnostic purposes. *Appl Phys B* 50:487–497.
22. Huang Y-L, Gordon RJ (1992) The effect of amplified spontaneous emission on the measurement of the multiplet state distribution of ground state oxygen atoms. *J Chem Phys* 97:6363–6368.
23. Luo Q, Liu W, Chin SL (2003) Lasing action in air induced by ultra-fast laser filamentation. *Appl Phys B* 76:337–340.
24. Agrup S, Aldén M (1994) Two-photon laser-induced fluorescence and stimulated emission measurements from oxygen atoms in a hydrogen/oxygen flame with picosecond resolution. *Opt Commun* 113:315–323.
25. Sanchez-Gonzalez R, Srinivasan R, Bowersox RDW, North SW (2011) Simultaneous velocity and temperature measurements in gaseous flow fields using the VENOM technique. *Opt Lett* 36:196–198.
26. Scully MO, Zubairy MS (1997) *Quantum Optics* (Cambridge Univ Press, New York).
27. Dyer MJ, Crosley DR (1989) Doppler-free laser-induced fluorescence of oxygen atoms in an atmospheric-pressure flame. *Opt Lett* 14:12–14.
28. Allen L, Eberly JH (1987) Optical Resonance and Two Level Atoms. (Dover, New York).

29. MacGillivray JC, Feld MS (1976) Theory of superradiance in an extended, optically thick medium. *Phys Rev A* 14:1169–1189.
30. Paradis E, Barrett B, Kumarakrishnan A, Zhang R, Raithel G (2008) Observation of superfluorescent emissions from laser-cooled atoms. *Phys Rev A* 77:043419.
31. Maki JJ, Malcuit MS, Raymer MG, Boyd RW, Drummond PD (1989) Influence of collisional dephasing processes on superfluorescence. *Phys Rev A* 40:5135–5142.
32. Wang CY, et al. (2007) Coherent instabilities in a semiconductor laser with fast gain recovery. *Phys Rev A* 75:031802.
33. Brownell JH, Lu X, Hartmann SR (1995) Yoked superfluorescence. *Phys Rev Lett* 75:3265–3268.
34. Yuan L, Svidzinsky AA (2012) Gain without population inversion in a yoked superfluorescence scheme. *Phys Rev A* 85:033836.